

Patterns of ocean current variability on the West Florida Shelf using the self-organizing map

Yonggang Liu and Robert H. Weisberg

College of Marine Science, University of South Florida, St. Petersburg, Florida, USA

Received 22 October 2004; revised 9 February 2005; accepted 17 March 2005; published 10 June 2005.

[1] Patterns of ocean current variability are examined on the West Florida Shelf by a neural network analysis based on the self-organizing map (SOM), using time series of moored velocity data that span the interval October 1998–September 2001. Three characteristic spatial patterns are extracted in a 3×4 SOM array: spatially coherent southeastward and northwestward flow patterns with strong currents and a transition pattern of weak currents. On the synoptic weather timescale the variations of these patterns are coherent with the local winds. On the seasonal timescale the variations of the patterns are coherent with both the local winds and complementary sea surface temperature patterns. The currents are predominantly southeastward during fall–winter months (from October to March) and northwestward during summer months (from June to September). The spatial patterns extracted by the (nonlinear) SOM method are asymmetric, a feature that is not captured by the (linear) empirical orthogonal function method. Thus we find for the synoptic weather and longer timescales that (1) southeastward currents are generally stronger than northwestward currents, (2) the coastal jet axis is located further offshore for southeastward currents than for northwestward currents, and (3) the velocity vector rotations with depth are larger in shallower water when the currents are southeastward relative to when the currents are northwestward.

Citation: Liu, Y., and R. H. Weisberg (2005), Patterns of ocean current variability on the West Florida Shelf using the self-organizing map, *J. Geophys. Res.*, 110, C06003, doi:10.1029/2004JC002786.

1. Introduction

[2] Most previous observational studies of West Florida Shelf (WFS) currents are based on limited current meter measurements, either over short time periods within a particular season or located relatively far offshore [Niiler, 1976; Weatherly and Martin, 1978; Blaha and Sturges, 1981; Mitchum and Sturges, 1982; Cragg *et al.*, 1983; Marmorino, 1982, 1983a, 1983b; Mitchum and Clarke, 1986; Halper and Schroeder, 1990; Weatherly and Thistle, 1997]. These studies generally offer little information on either the spatial patterns or the seasonal variability of the water motions over the shelf. Longer records with higher vertical resolution were initiated on the WFS in 1993 using acoustic Doppler current profilers (ADCP). On the basis of velocity data collected at the 47 m isobath from October 1993 through January 1995, a seasonal cycle of the monthly mean currents was hypothesized to be driven by a seasonally varying shelf-wide baroclinic structure along with the winds [Weisberg *et al.*, 1996]. More recent and more extensive coverage by ADCP moorings over the inner shelf are available from June 1998 through December 2001, facilitating a systematic analysis of the spatial patterns of ocean current variability, which is the subject of our paper.

Various analysis techniques are available, including conventional empirical orthogonal functions (EOF) and neural networks. Here we employ both of these techniques and compare their results.

[3] As an artificial neural network based on unsupervised learning, the self-organizing map (SOM) is an effective software tool for detecting patterns in large data sets [Kohonen, 1982, 2001]. SOM is a nonlinear cluster analysis mapping high-dimensional input data onto a (usually) two-dimensional output space while preserving the topological relationships between the input data. As a pattern recognition and classification tool, the SOM finds widespread use across a number of disciplines [Kaski *et al.*, 1998; Oja *et al.*, 2002]. Since its first climate application by Hewitson and Crane [1994], the SOM has gained acceptance in climate and meteorological research [Malmgren and Winter, 1999; Cavazos, 2000; Ambroise *et al.*, 2000; Hewitson and Crane, 2002; Hsu *et al.*, 2002; Hong *et al.*, 2004, 2005]. The SOM has also been applied in oceanography by Ainsworth [1999] and Ainsworth and Jones [1999] for chlorophyll estimates from satellite data, by Silulwane *et al.* [2001] and Richardson *et al.* [2002] to identify ocean chlorophyll profiles, by Hardman-Mountford *et al.* [2003] to relate satellite altimeter data with the recruitment of the Namibian sardine, by Ultsch and Röske [2002] to predict sea level, and by Richardson *et al.* [2003] and Risien *et al.* [2004] to extract sea surface temperature (SST) and wind patterns from satellite data.

[4] In this paper, the SOM is applied to moored ADCP data to extract the spatial patterns of ocean current variations on the WFS. The purposes are twofold: (1) to describe the characteristic current patterns and their temporal variations and (2) to demonstrate the usefulness of the SOM Toolbox for such oceanographic applications.

[5] The paper is arranged as follows. Since the SOM is relatively new to oceanography, a brief description of the technique is given in section 2. Section 3 then describes the data. Applications of the linear EOF and nonlinear SOM methods are made in sections 4 and 5, respectively, where we find fundamental differences in the revealed patterns. Section 6 discusses these synoptic and seasonally varying current patterns and summarizes the results.

2. Self-Organizing Map (SOM) and the SOM Toolbox

[6] The SOM is a nonlinear, ordered, smooth mapping of high-dimensional input data onto the elements of a regular, low-dimensional (usually two-dimensional) array (for more detailed discussions, see *Kohonen* [1982, 2001]). The SOM consists of a set of i units arranged in a two-dimensional grid with a weight vector \mathbf{m}_i attached to each unit that may be initialized randomly. During the self-organizing process (e.g., the sequential training), elements from the high-dimensional input space, referred to as input vectors \mathbf{x} , are presented to the SOM and the activation of each unit for the presented input vector is calculated. Commonly, it is the Euclidian distance between the weight vector of the unit and the input vector that serves as the activation function. The weight vector of the unit showing the highest activation (i.e., the smallest Euclidian distance) is selected as the “winner,” c_k , and is modified to more closely resemble the presented input vector:

$$c_k = \arg \min \|\mathbf{x}_k - \mathbf{m}_i\|. \quad (1)$$

[7] The weight vector of the winner is moved toward the presented vector by a certain fraction of the Euclidean distance as indicated by a time-decreasing learning rate α . The learning rate α can be specified by a linear, power, or inverse time function:

$$\alpha(t) = \begin{cases} \alpha_0(1 - t/T), & \text{linear} \\ \alpha_0(0.05/\alpha)^{t/T}, & \text{power} \\ \alpha_0/(1 + 100t/T), & \text{inverse} \end{cases} \quad (2)$$

where T is the training length, and α_0 is the initial learning rate. In the SOM Toolbox, the default is a linear function, and the default α_0 is 0.5 for an initial rough training session and 0.05 for further fine tuning. Users may also provide initial and final α values, or specify other time decreasing functional forms. Thus the winner’s activation will be even higher the next time the same vector is presented. Also, the weight vectors of units in the neighborhood of the winner are modified according to a spatiotemporal neighborhood function ε , that, similar to the learning rate, is a time-decreasing function. Also, ε decreases spatially away from the winner. There are four types of neighborhood function

available in the SOM Toolbox: “bubble,” “gaussian,” “cutgauss,” and “ep”:

$$\varepsilon_{ci}(t) = \begin{cases} F(\sigma_t - d_{ci}), & \text{bubble} \\ \exp(-d_{ci}^2/2\sigma_t^2), & \text{gaussian} \\ \exp(-d_{ci}^2/2\sigma_t^2)F(\sigma_t - d_{ci}), & \text{cutgauss} \\ \max\{0, 1 - (\sigma_t - d_{ci})^2\}, & \text{ep} \end{cases} \quad (3)$$

where σ_t is the neighborhood radius at time t , d_{ci} is the distance between map units c and i on the map grid and F is a step function:

$$F(x) = \begin{cases} 0 & \text{if } x < 0 \\ 1 & \text{if } x \geq 0. \end{cases} \quad (4)$$

The default neighborhood function in the SOM Toolbox is “gaussian.” The neighborhood radius σ_t also decreases as a function of time along with the learning rate α . The learning rule, incorporating α and ε is

$$\mathbf{m}_i(t+1) = \mathbf{m}_i(t) + \alpha(t) \cdot \varepsilon(t) \cdot [\mathbf{x}(t) - \mathbf{m}_i(t)], \quad (5)$$

where t denotes the current learning iteration and \mathbf{x} represents the currently presented input vector. This learning procedure leads to a topologically ordered mapping of the presented input vectors. By virtue of the neighborhood function similar patterns are mapped onto neighboring regions on the map, while dissimilar patterns are mapped farther apart.

[8] Most of the previously referenced SOM applications in meteorology and oceanography are based on a software package SOM_PAK 3.1 or earlier versions [*Kohonen et al.*, 1995] (available at http://www.cis.hut.fi/research/som_pak), all written in C language. Recently, a more user friendly implementation of the SOM as a MATLAB Toolbox has been provided by *Vesanto et al.* [2000]. The SOM toolbox version 2.0 can be downloaded from the Helsinki University of Technology, Finland: <http://www.cis.hut.fi/projects/somtoolbox>.

3. Data

[9] Among the WFS moorings (Figure 1), five are bottom-mounted and located between the 10 m to 25 m isobaths, each with an upward looking ADCP measuring the water column currents at 0.5 m intervals. From the 25 m to 50 m isobaths, there are six surface buoys, each with a downward-looking ADCP, similarly measuring the water column currents. Most of these moorings have been maintained with multiple deployments for more than 3 years (Figure 2), and the period October 1998 through September 2001 selected for analysis has the greatest commonality of data. Additional information on the moorings and the data editing are given by *Liu and Weisberg* [2005].

[10] Near-surface, middepth, and near-bottom velocity data are extracted from each profile so that each of the mooring sites is given equal weight in the analyses. All of the hourly velocity data are then low-pass filtered to eliminate oscillations on timescales shorter than 2 days, such as tides and inertial motions. The temporal mean and the principal axis currents at these three levels, averaged

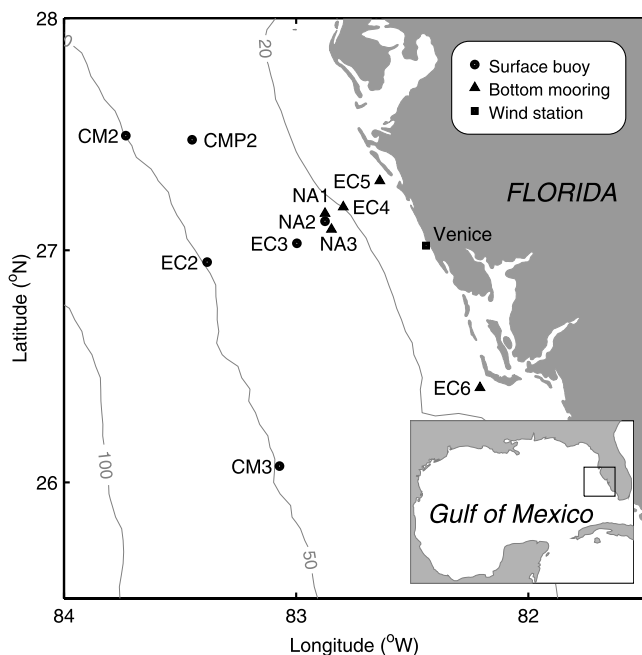


Figure 1. Map of the West Florida Shelf showing topography (isobaths units in m), acoustic Doppler current profiler (ADCP) moorings, and wind stations. A map of the whole Gulf of Mexico is inserted in the lower right corner, and the square box designates our study area.

from October 1998 to September 2001 are shown in Figure 3. The mean currents tend to be along isobath and southeastward, and they are much weaker in amplitude than the current fluctuations. The principal axes also tend to align with the isobaths, and the ratios of the minor to major axes of the variance ellipses vary from 0.2 (at the 10 m isobath) to 0.7 (at the 50 m isobath). The ellipse orientations tend to rotate anticlockwise from the surface down to the bottom, with these net angular offsets increasing with increasing water depth.

4. Empirical Orthogonal Function Patterns

[11] Before performing SOM analyses, we begin with the established technique of time domain EOF [e.g., Richman, 1986; Lagerloef and Bernstein, 1988; He et al., 2003;

Espinosa-Carreón et al., 2004]. EOF analysis is the same as principal component (PC) analysis [Hotelling, 1933]. Here we refer to the PCs as the amplitudes, which are functions of time, of their corresponding spatial eigenfunctions, or EOFs. The analysis separates the data set into data-dependent, empirical orthogonal modes. Generally speaking, each mode n has an associated variance, a dimensional spatial pattern $F_n(x)$, and a nondimensional time series $\alpha_n(t)$. Thus the EOF representation of velocity anomalies is

$$V(x, t) = \sum_{n=1}^N \alpha_n(t) F_n(x). \quad (6)$$

[12] EOF analysis requires the input data to be continuous. CMP2 data is the shortest record, and it is only used to replace the gaps in the CM2 data, as the two sites are in close proximity. Data gaps in the other records are filled through linear regression from adjacent stations. We perform the analysis by arranging the velocity time series in a two-dimensional array such that each velocity snapshot is in a single row vector and the time series of each velocity component is in a single column. All u components are placed in the first half of the rows followed by all v components. Thus the input matrix consists of 60 columns (10 stations \times 3 levels \times 2 components) \times 25585 rows (hours). The temporal mean values are removed prior to the EOF analysis.

[13] The first EOF mode accounts for 65.0% of the subtidal velocity variance. The eigenvector shows a coherent pattern of along-shelf flows shoreward of the 50 m isobath (Figure 4). The currents tend to be along isobath at the mid levels, whereas they tend to turn onshore at the near-surface level and offshore at the near-bottom level. That is, the current vectors rotate counterclockwise from the surface down to the bottom, and this rotation is more pronounced in deeper water. Thus relative to the shoreline, for downwelling the horizontal flow field pattern tends to be convergent at the near-surface and mid levels, and divergent at the near-bottom level, and conversely for upwelling. The alongshore component tends to be largest around the 25 m to 30 m isobaths, indicative of a coastal jet. This is consistent with the coastal jet structure obtained in a constant density numerical model simulation for the WFS [Li and Weisberg, 1999]. The associated PC shows the temporal variation of this spatial pattern, which occurs at

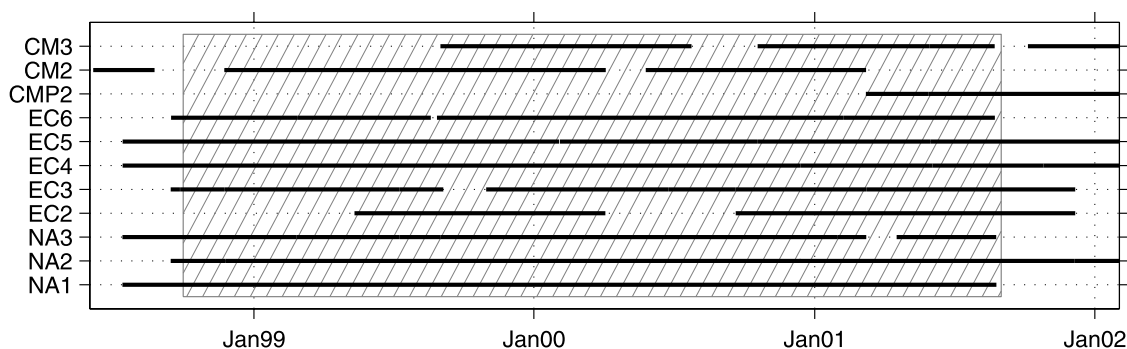


Figure 2. Time line of the ADCP mooring records. The hatched area shows the time domain of the data on which this study is based.

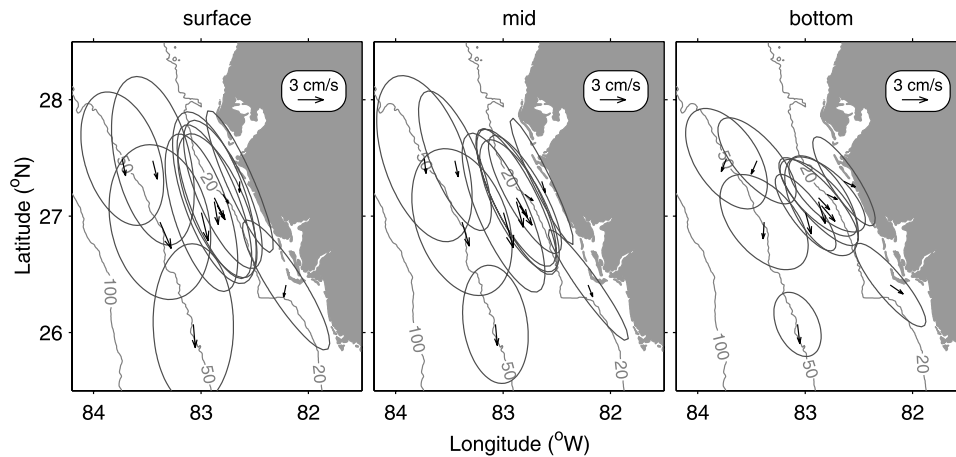


Figure 3. Mean and principal axis currents at the (left) near-surface, (center) mid, and (right) near-bottom levels, averaged from 2 day low-pass filtered data from October 1998 through September 2001. Note that the mean currents are much weaker than their deviations.

both synoptic weather and seasonal timescales. In fall-winter (summer) this first mode PC tends to be negative (positive) indicating that the inner shelf currents tend to be southeastward (northwestward). These PC variations are visually coherent with the local winds, suggesting that the local winds are the main driving force for the currents

over the inner shelf, and this is consistent with the observed turning in the implied surface and bottom Ekman layers.

[14] The second mode spatial pattern (not shown) consists of northwestward currents along the 50 m isobath and southeastward currents near the coast, indicating an inner

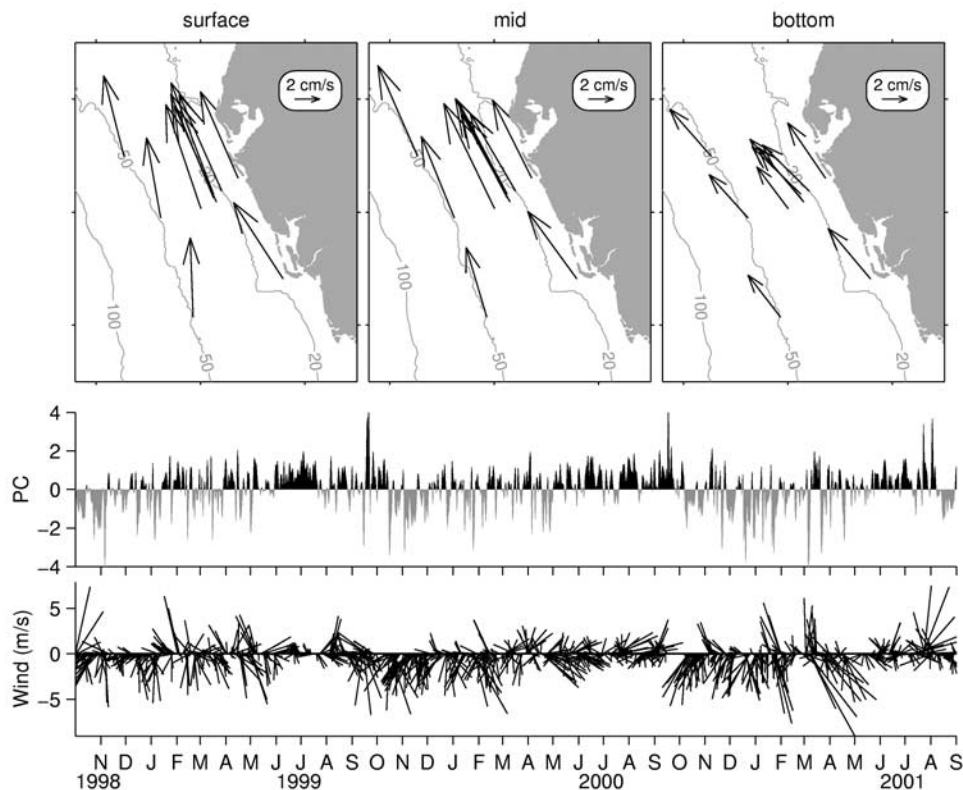


Figure 4. Time domain empirical orthogonal function (EOF) analysis of the 2 day low-pass filtered currents at the three levels from October 1998 through September 2001. (top) First mode eigenvectors. (middle) First mode PC time series. (bottom) Five day low-pass filtered, daily subsampled winds at Venice station. The first mode EOF accounts for 65.0% of total variance.

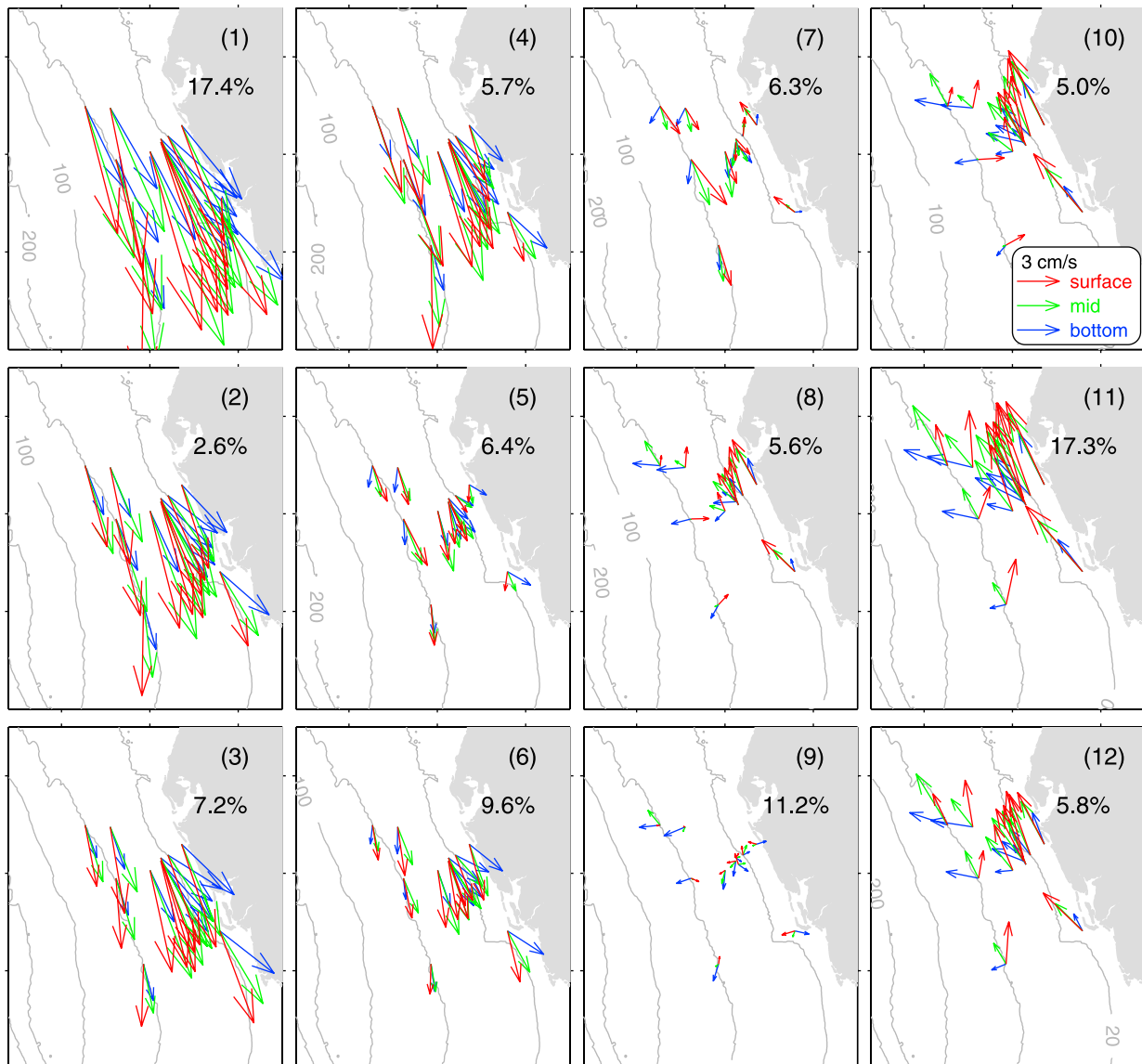


Figure 5. A 3×4 self-organizing map (SOM) of the 2 day low-pass filtered velocity data at the three levels from October 1998 through September 2001. The relative frequency of occurrence of each pattern is shown in the upper right corner of each map.

shelf shear structure. It only accounts for 6.4% of the total variance. Since these patterns contain both the synoptic and seasonal scales, further low-pass filtering does not affect them much.

5. SOM Patterns

[15] The same data are used for the SOM analysis except that the data gaps are ignored and data from moorings CM2 and CMP2 are treated as two separate time series. Thus the input matrix consists of 66 columns ($11 \text{ stations} \times 3 \text{ levels} \times 2 \text{ components}$) \times 25585 rows. Also, the temporal mean values are retained. The size of the SOM array must be specified prior to the training process. After several test runs, an SOM size of 3×4 was selected. This is large enough to represent the character-

istic velocity features and small enough to be visualized and interpreted.

5.1. SOM Array

[16] The 3×4 SOM array results are shown in Figure 5. The left-hand side of the array is populated by spatially coherent southeastward currents, while the right-hand side shows coherent northwestward currents. Similar velocity patterns are located adjacent to one another in this SOM mapping, while dissimilar patterns are at opposite ends of the SOM space, with a continuum of change occurring across the array. For each time frame (spatial snapshot) of the velocity time series, the best matching unit (BMU), or the “winner,” can be identified according to the minimum Euclidian distance when that frame is compared to the 12 SOM units. Similarly, the second and/or third BMU

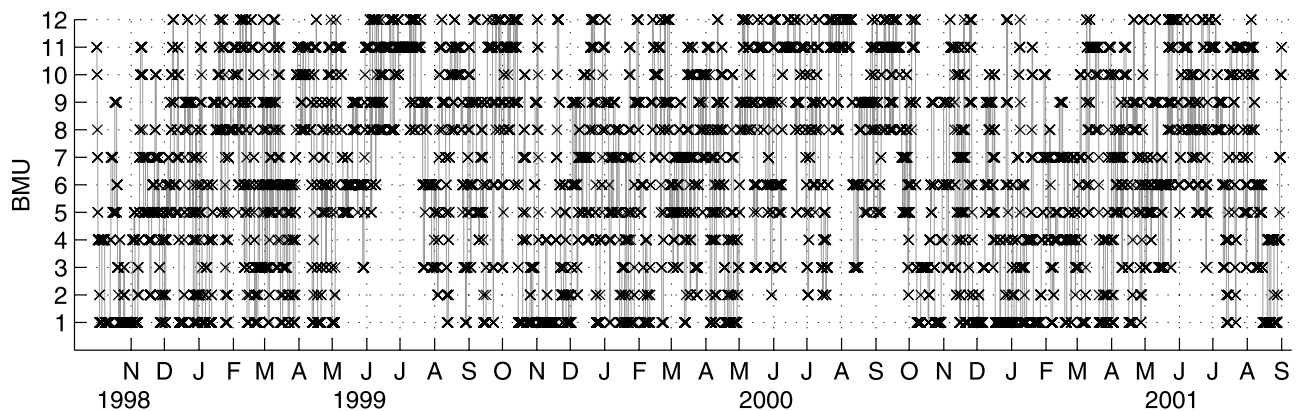


Figure 6. Temporal evolution of the best matching unit (BMU) for the 3×4 SOM. The tick marks on the vertical axis correspond to the pattern numbers in the SOM (Figure 5).

may also be identified; usually, they are the SOM units adjacent to the BMU in the SOM space. Hourly time series of the BMU for the input data is shown in Figure 6. The temporal evolution of the BMU is coarse in Figure 6, as the input velocity data (2 day low-pass filtered) includes both the synoptic and seasonal variations. For a synoptic event, the BMU may switch back and forth between patterns in a matter of days. In order to quantify the representation of each unit, the frequency of occurrence is computed by summing the number of selections of that unit (the BMU) divided by the total record length (the number of input vectors). The relative frequency of occurrence of each unit is shown in the upper right corner of each map in Figure 5. Thus the SOM unit 1 represents 17.4% of the input (subtidal) currents, showing a pattern with the strongest southeastward currents. Its opposite counterpart, unit 11, represents 17.3% of the data, showing a pattern with the strongest northwestward currents.

5.2. Synoptic Variability

[17] The synoptic-scale variations of the input velocity data from the BMU evolution are better viewed by focusing in on specific time periods. As examples we choose four representative months (December 1998, August 1999, March 2000 and June 2000), as shown in Figure 7 with the BMU plotted along with the wind time series. From the BMU we see the preference for units 1–6 when the local winds are upwelling favorable (directed southward), versus units 10–12 when the winds are downwelling favorable (directed northward). Thus the SOM units 1–6 represent characteristic upwelling flow patterns, while the units 10–12 represent characteristic downwelling flow patterns. Units 7–9 are transitional patterns. Note that the change of the BMU is highly coherent with the local winds, suggesting that the main driving force for the currents on the inner shelf over the synoptic weather band is the local winds, consistent with the WFS numerical model findings [e.g., *He et al.*, 2004].

[18] We note that the upwelling and downwelling patterns extracted by the SOM are asymmetric (Figure 5). The currents in the upwelling patterns are generally stronger than those in the downwelling patterns, and the coastal jet is located around the 25 m to 30 m isobaths in the upwelling

patterns, whereas it is located closer to the coast at the shallowest 10 m station in the downwelling patterns. Moreover, the velocity vector rotation with depth differs among the upwelling and downwelling patterns. In the upwelling patterns, the angular offset of about 10° along the 50 m isobath is smaller than the 20° offset at the 10 m isobath, i.e., the rotation increases toward the coast. The downwelling patterns, in contrast, have angular offsets decreasing toward the coast. These asymmetric behaviors cannot be identified in a linear EOF analysis.

5.3. Seasonal Variability

[19] Although masked by the synoptic variations, the seasonal variations may still be identified in Figure 6. For example, if measured in terms of BMU selectivity, the probability of units 10–12 is low during fall–winter (from November through March), and similarly, the probability of units 1–6 is low during summer (from June to September). To better illustrate this, we calculated the climatological monthly mean frequency of occurrence of the three characteristic sets of patterns in the SOM (Figure 8). Units 1–6 dominate the winter half year from October through May, with peak frequency of occurrence in October, and units 10–12 dominate the summer months (June, July and September). The transition patterns, units 7–9, may occur in all the months, but with lower frequency of occurrence. Thus units 1–6 represent the characteristic fall–winter patterns, whereas units 10–12 represent the characteristic summer patterns.

[20] To better describe the seasonal variation, 15 day low-pass filtered velocity data are used as input to the same SOM calculations. Similar to those of the 2 day low-pass filtered results, the 3×4 SOM shows three sets of flow patterns (Figures 9 and 10). In the fall–winter patterns, the currents tend to be southeastward in along-shelf direction with a coastal jet located around the 30 m isobath. The near-bottom currents have obvious onshore component near-shore. In the summer patterns, the currents are weaker. However, they are northwestward on the inner shelf with a weak current core around the 20–25 m isobaths.

[21] This SOM representation of the seasonal cycle is consistent with a monthly mean velocity climatology averaged from October 1998 to September 2001 shown in

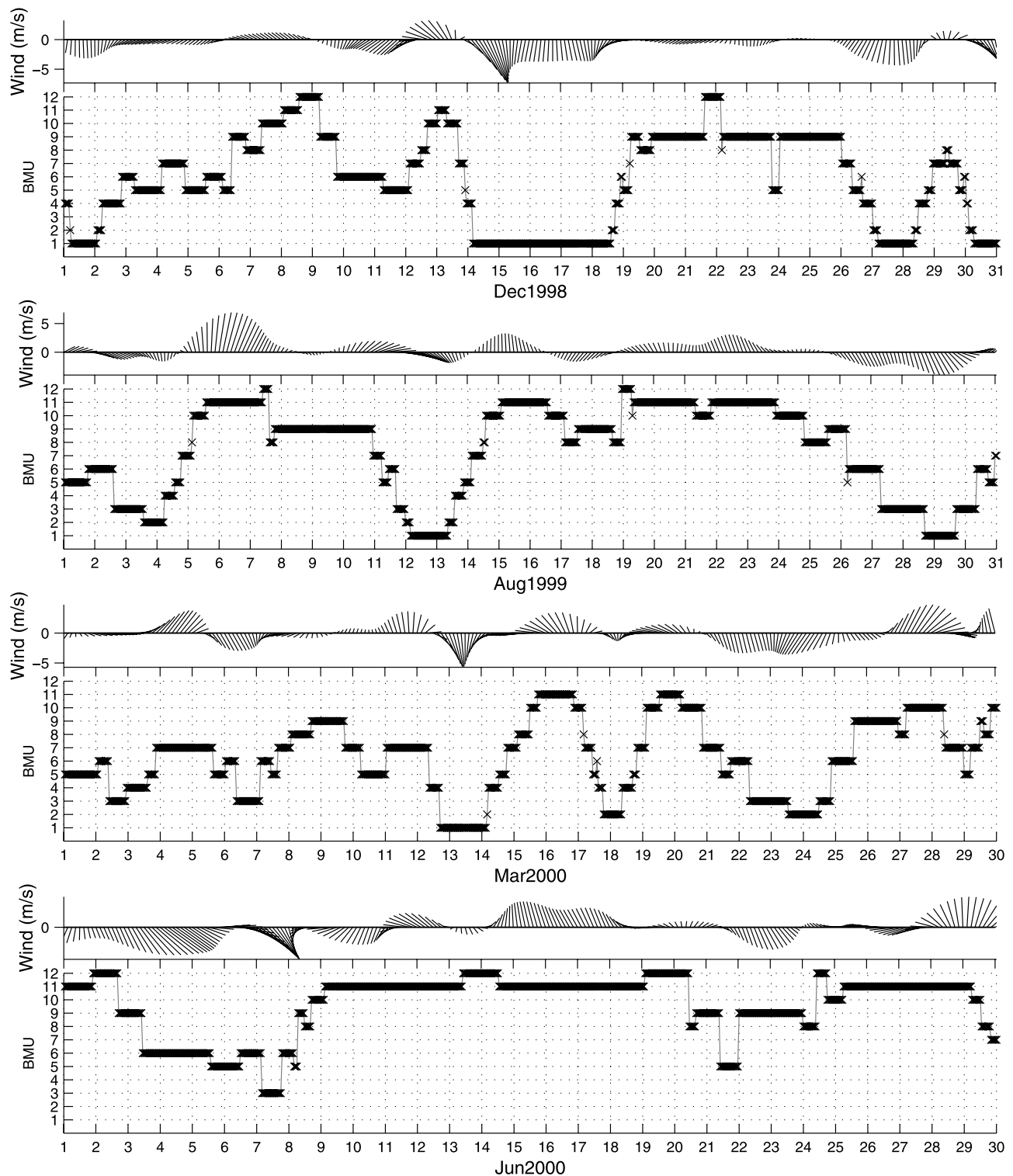


Figure 7. Time series of the Venice winds and the BMU for the 3×4 SOM during four separate months: (top to bottom) December 1998, August 1999, March 2000, and June 2000. The wind data were 2 day low-pass filtered and were subsampled at 3 hour intervals.

Figure 11. From October through April, the mean currents are southeastward, with the strongest currents in January. Following a transition in May, the mean currents turn northwestward from June through September, but with

weaker or even southeastward currents in August. In fall–winter months, the near-bottom currents generally have an onshore component on the inner shelf, and the coastal jet is located around 25–30 m isobaths. In the summer months

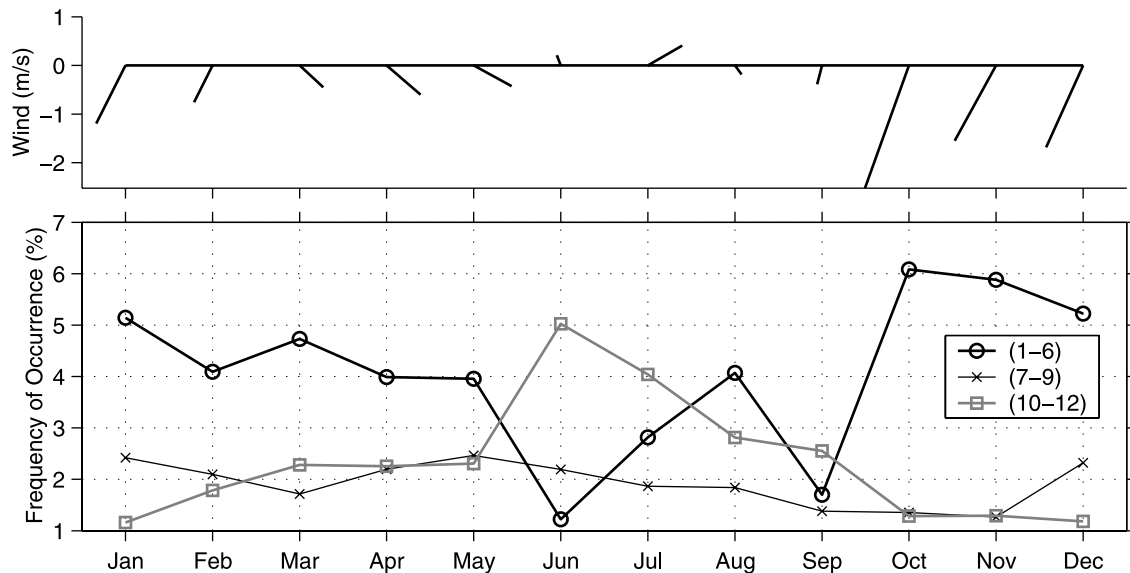


Figure 8. Climatological monthly mean winds and frequency of occurrence of the three characteristic patterns in the SOM, averaged over the 3 year period October 1998–September 2001.

(June–July), the coastal jet is located around the 20–25 m isobaths. These findings compare well with those of the 15 day low-pass filtered SOM results.

[22] The climatological monthly mean winds are strong and southward from October to January, which may partially explain the occurrence of the fall–winter current patterns during those months (Figure 8). The mean winds are northward in June and July, which may partially explain the presence of the summer patterns in those 2 months. The fact that the fall–winter mean winds are much stronger than the summer mean winds helps to explain the asymmetric strengths of the currents in the fall–winter and summer seasons.

[23] Overlaid on these (Figure 11) maps is the monthly mean SST climatology (composited using the 5 year daily optimum interpolation product from 1998 to 2002 of *He et al.* [2003]). *Liu et al.* [2005] performed a spatial analysis on these SST data. Here we point out that the seasonal variation of the currents is consistent with that of the SST. In winter months, the SST is lower along the coast and higher in the deep ocean area, with a horizontal temperature gradient approximately pointing onshore in the across-shelf direction. This winter SST pattern results in a density-induced baroclinic current flowing along-shelf toward the southeast, which would add constructively with the southeastward wind-driven current. The monthly mean SST gradient is generally not as obvious in summer. However, there is a warm tongue located over the mid shelf in August, which favors a southeastward current on the inner shelf. Whether or not baroclinicity by this warm tongue impacts the August current patterns remains to be addressed.

5.4. Interannual Variation

[24] Our analysis shows that in August, the southward flow patterns outnumber the northward flow patterns (Figure 8), consistent with the climatological monthly mean currents (Figure 11). This August reversal warrants further study. We calculate the monthly mean frequency of occur-

rence of the three characteristic patterns, and show the time series in Figure 12. Note that since the calculation is based on 35 months, it is not surprising that the values of the frequency of occurrence for individual months are small (<2.5%). We note that the summation of all values in Figure 12 equals 100%. In August 1999 both the southward and northward patterns have about the same frequencies of occurrence. In August 2000, the northward patterns outnumber the southward patterns by 0.5% in the frequency of occurrence. However, in August 2001 the southward patterns outnumber the northward patterns by 1.5%. An average of the numbers across these 3 years results in the preferred southward current pattern. This raises the question on whether the August reversal derives from interannual variability as opposed to being a robust feature of the annual cycle.

[25] Interannual variation of the three dominant composite current patterns is seen during these 3 years. The total frequency of occurrence of the southeastward flow patterns (1–6) during the winter half year (October through March) is 10.8%, 9.2% and 11.2% in 1998–1999, 1999–2000 and 2000–2001, respectively; and that of the northwestward flow patterns (10–12) in summer (June and July) is 3.6%, 3.0% and 2.5% in 1999, 2000 and 2001, respectively. These interannual changes may be related to interannual variations in either the local (e.g., winds, Figure 12), deep ocean forcing, or some combination thereof [*Weisberg et al.*, 2005]. Additional data being collected will eventually be able to describe these interannual variations more clearly, and this highlights the need for long time series as part of the evolving coastal ocean observing systems that are presently under consideration.

6. Discussion and Summary

[26] We applied both linear EOF and nonlinear neural network (based on the SOM) analyses to examine characteristic patterns of the ocean current variability on the inner

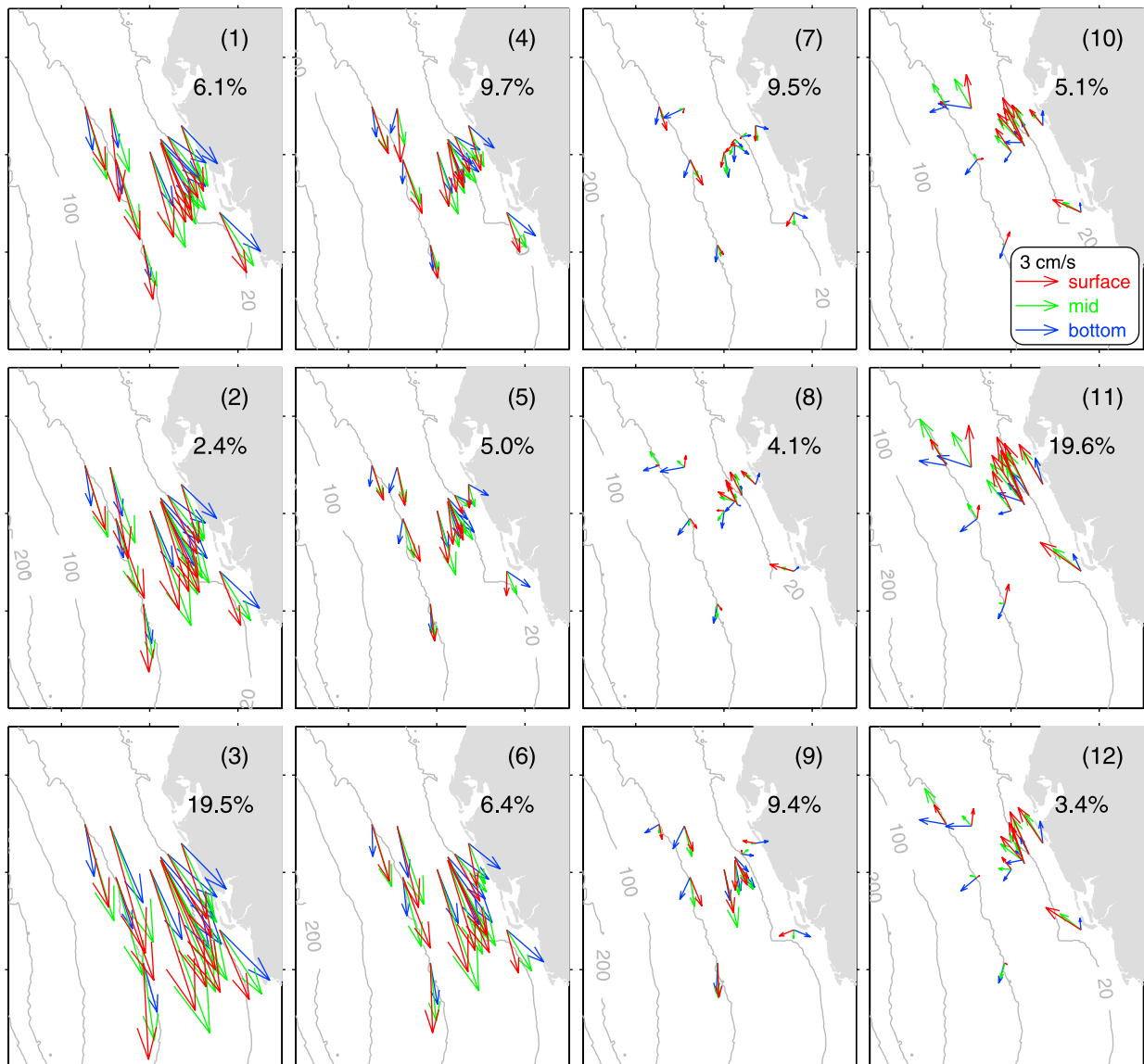


Figure 9. Same as Figure 5, except for the 15 day low-pass filtered velocity data.

WFS, using moored (ADCP) velocity time series that span the 3 year interval October 1998 to September 2001. The first mode EOF shows a coherent spatial pattern of along-shelf currents with a coastal jet centered around the 25 m to

30 m isobaths, varying in time (as given by the fluctuating PC time series) on both synoptic and seasonal timescales. These spatial and temporal patterns are such that the currents tend to flow southeastward in winter and north-

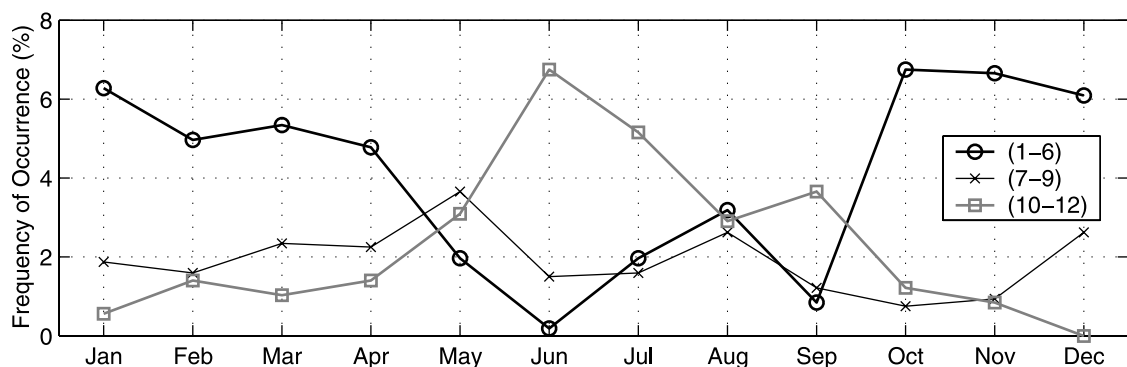


Figure 10. Same as Figure 8, except for the 15 day low-pass filtered velocity data.

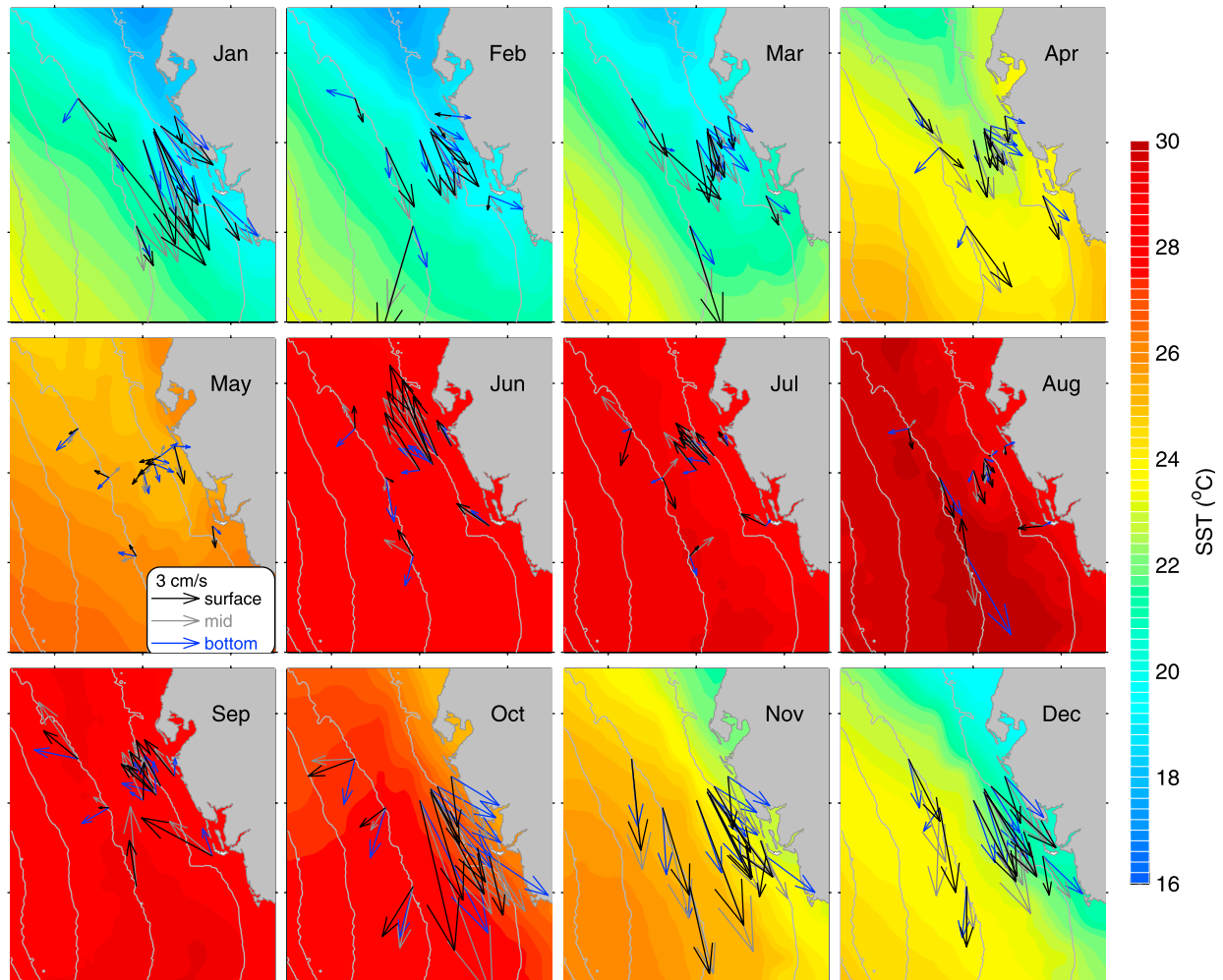


Figure 11. Climatological monthly mean sea surface temperature (SST) superimposed with the currents at the near-surface, mid, and near-bottom levels. The SST data were averaged from 5 year daily maps, 1998–2002; the currents were averaged from 2 day low-pass filtered data, October 1998–September 2001.

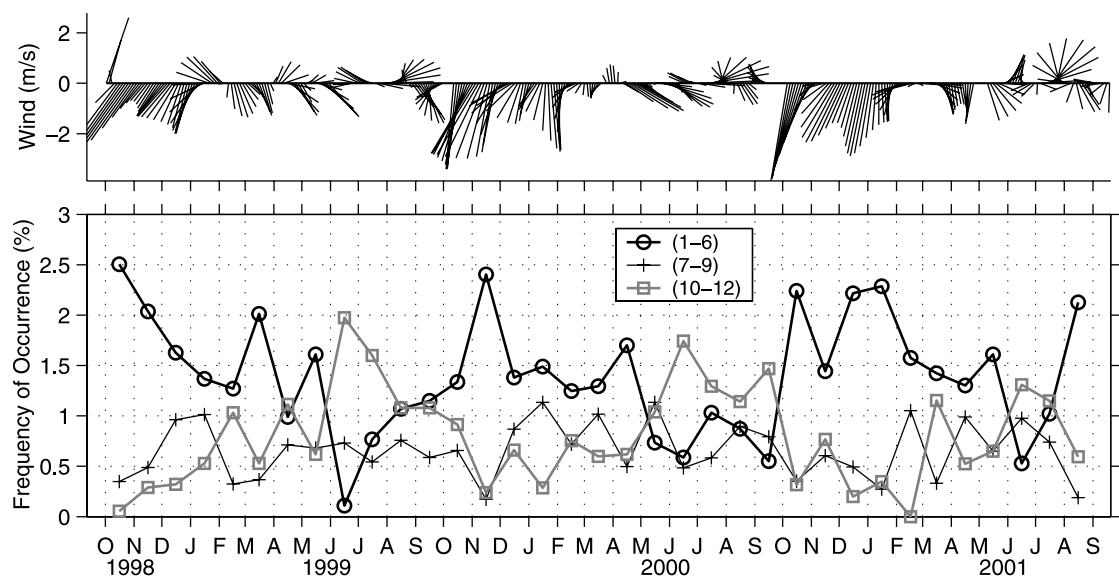


Figure 12. Monthly mean frequency of occurrence of the three characteristic patterns in the (bottom) SOM and the (top) Venice winds. The wind data were 30 day low-pass filtered and 3 day subsampled.

westward in summer, with an anticlockwise vertical rotation from the surface down to the bottom consistent with Ekman and geostrophic dynamics. Similar current reversals also occur on synoptic scales in response to the wind reversals.

[27] A 3×4 SOM array also shows characteristic current patterns. These group into three composite categories: southeastward and northwestward flow patterns with strong currents, and transitional patterns with weak currents. The synoptic, seasonal, and interannual variations of these current patterns are shown using different arrangements of the BMU time series. The synoptic variations of the currents are coherent with the local winds. The seasonal variation of the currents is coincident with the variations of both the local winds and the seasonal SST patterns. The currents are dominantly southeastward during fall–winter months (from October to March), and northwestward during summer months (from June through September), although an anomaly occurs in August that may be due to interannual variations in winds or deep ocean influence. The summer currents tend to be weaker than the fall–winter currents.

[28] Both the EOF and SOM techniques are very useful in extracting current patterns. The linear EOF, ordered on variance reduction, form a complete set from which the data may be identically reconstructed. The nonlinear SOM, minimizing Euclidian distance between learned pattern vectors and data vectors, preserves the data topology rather than the variance. While the data may not be identically reconstructed the resulting patterns may be more like the data than any of the leading EOFs. Hence for pattern recognition and description the SOM may have advantage over the EOF.

[29] A significant finding identified herein by the SOM, and not by the EOF, is that the patterns of current variability are asymmetric with respect to upwelling (southeastward) and downwelling (northwestward) flows. At the synoptic weather and longer timescales, the currents in the upwelling patterns are generally stronger than those in the downwelling patterns, and the coastal jet is located around the 25 m to 30 m isobaths in the upwelling patterns, whereas it is located closer to the coast at the shallowest 10 m isobath station in the downwelling patterns. Moreover, the velocity vector rotations with depth differ among the upwelling and downwelling patterns. In the upwelling patterns, the angular offset of about 10° along the 50 m isobath is smaller than the 20° offset at the 10 m isobath, i.e., the rotation increases toward the coast. The downwelling patterns, in contrast, have angular offsets decreasing toward the coast. Similarly, on the seasonal timescale, the currents in the fall–winter (upwelling) patterns are much stronger than those in the summer (downwelling) patterns, but the coastal jet for both of these winter and summer patterns is located around the 20 m to 30 m isobaths. Asymmetry on the seasonal timescale is in part explained by stronger winds in fall–winter than in summer. However, in contrast with the seasonal timescale, the wind reversals at the synoptic timescale are of comparable values. Asymmetry at the synoptic scale has a basis in model simulation as well as in the observations [Weisberg *et al.*, 2001], where under stratified conditions thermal wind effects lead to disproportionately larger responses (in both magnitude and offshore scale) for upwelling favorable winds over downwelling favorable winds.

[30] Another attribute of the SOM is that the temporal mean does not have to be removed prior to the analysis, allowing the output patterns to be visualized in the same form as the original data. This advantage is not that obvious in our analysis, because the temporal mean currents are much weaker than their deviations. However, it is very useful when the temporal mean values are larger, for instance, in sea surface temperature analyses [Richardson *et al.*, 2003; Liu *et al.*, 2005].

[31] Finally, the self-organizing algorithm handles missing data without a priori estimation. From this point of view, the (nonlinear) SOM is more convenient to use than the (linear) EOF.

[32] One limitation of the SOM is that its size (arrangement of the neurons) needs to be specified before the training process, and this is arbitrary. A larger map (more neurons) extracts more detailed information, whereas a smaller map (less neurons) returns more general information. A set of test runs were performed, and slightly different patterns were obtained. However, all of these patterns can be grouped to the same three characteristic categories as presented in this paper. The training length T (i.e., number of iterations) also affects the outcome. Small values (e.g., $T = 1$) lead to underestimated velocities, whereas large values ($T > 10$) give almost the same results. Different learning rates and spatial functions were tested, almost identical results were found when the training length was greater than 10. With the same training length, we found the “batch” training to be the fastest algorithm, and the sequential training to be the slowest.

[33] **Acknowledgments.** Support was by the Office of Naval Research, grants N00014-98-1-0158 and N00014-02-1-0972. The second of these, for the Southeast Atlantic Coastal Ocean Observing System (SEACOOS), is administered by UNC under Task order 3-12110-10. The USF Ocean Circulation Group assisted in all aspects of the data collection and analysis. Sea-going activity successes were largely owing to R. Cole and C. Merz. Data editing and analyses were aided by J. Donovan, R. Helber, and D. Mayer. The SOM MATLAB Toolbox was made by E. Alhoniemi, J. Himberg, J. Parhankangas, and J. Vesanto.

References

- Ainsworth, E. J. (1999), Visualization of ocean colour and temperature from multispectral imagery captured by the Japanese ADEOS satellite, *J. Visualization*, 2, 195–204.
- Ainsworth, E. J., and S. F. Jones (1999), Radiance spectra classification from the ocean color and temperature scanner on ADEOS, *IEEE Trans. Geosci. Remote Sens.*, 37, 1645–1656.
- Ambroise, C., G. Seze, F. Badran, and S. Thiria (2000), Hierarchical clustering of self-organizing maps for cloud classification, *Neurocomputing*, 30, 47–52.
- Blaha, J., and W. Sturges (1981), Evidence for wind-forced circulation in the Gulf of Mexico, *J. Mar. Res.*, 39, 771–733.
- Cavazos, T. (2000), Using self-organizing maps to investigate extreme climate events: An application to wintertime precipitation in the Balkans, *J. Clim.*, 13, 1718–1732.
- Cragg, J., G. Mitchum, and W. Sturges (1983), Wind-induced sea-surface slopes on the West Florida shelf, *J. Phys. Oceanogr.*, 13, 2201–2212.
- Espinosa-Carreón, T. L., P. T. Strub, E. Beier, F. Ocampo-Torres, and G. Gaxiola-Castro (2004), Seasonal and interannual variability of satellite-derived chlorophyll pigment, surface height, and temperature off Baja California, *J. Geophys. Res.*, 109, C03039, doi:10.1029/2003JC002105.
- Halper, F. B., and W. W. Schroeder (1990), The response of shelf waters to the passage of tropical cyclones—Observations from the Gulf of Mexico, *Cont. Shelf Res.*, 10, 777–793.
- Hardman-Mountford, N. J., A. J. Richardson, D. C. Boyer, A. Kreiner, and H. J. Boyer (2003), Relating sardine recruitment in the Northern Benguela to satellite-derived sea surface height using a neural network pattern recognition approach, *Prog. Oceanogr.*, 59, 241–255.

- He, R., R. H. Weisberg, H. Zhang, F. Muller-Karger, and R. W. Helber (2003), A cloud-free, satellite-derived, sea surface temperature analysis for the West Florida Shelf, *Geophys. Res. Lett.*, **30**(15), 1811, doi:10.1029/2003GL017673.
- He, R., Y. Liu, and R. H. Weisberg (2004), Coastal ocean wind fields gauged against the performance of an ocean circulation model, *Geophys. Res. Lett.*, **31**, L14303, doi:10.1029/2003GL019261.
- Hewitson, B. C., and R. G. Crane (1994), *Neural Nets: Applications in Geography*, Springer, New York.
- Hewitson, B. C., and R. G. Crane (2002), Self-organizing maps: Applications to synoptic climatology, *Clim. Res.*, **22**, 13–26.
- Hong, Y., K. Hsu, S. Sorooshian, and X. Gao (2004), Precipitation estimation from remotely sensed imagery using an artificial neural network cloud classification system, *J. Appl. Meteorol.*, **43**, 1834–1853.
- Hong, Y., K. Hsu, S. Sorooshian, and X. Gao (2005), Self-organizing non-linear output (SONO): A neural network suitable for cloud patch-based rainfall estimation at small scales, *Water Resour. Res.*, **41**, W03008, doi:10.1029/2004WR003142.
- Hotelling, H. (1933), Analysis of a complex of statistical variables into principal components, *J. Educ. Psych.*, **24**, 417–441.
- Hsu, K.-L., H. V. Gupta, X. Gao, S. Sorooshian, and B. Imam (2002), Self-organizing linear output map (SOLO): An artificial neural network suitable for hydrologic modeling and analysis, *Water Resour. Res.*, **38**(12), 1302, doi:10.1029/2001WR000795.
- Kaski, S., J. Kangas, and T. Kohonen (1998), Bibliography of self-organizing map (SOM) papers: 1981–1997, *Neural Comput. Surv.*, **1**, 102–350.
- Kohonen, T. (1982), Self-organized information of topologically correct features maps, *Bio. Cyber.*, **43**, 59–69.
- Kohonen, T. (2001), *Self-Organizing Maps*, Springer Ser. Inf. Sci., vol. 30, 3rd ed., 501 pp., Springer, New York.
- Kohonen, J., J. Hynninen, J. Kangas, and J. Laaksonen (1995), SOM_PAK, the self-organizing map program, version 3.1, report, 27 pp., Helsinki Univ. of Technol. Lab. of Comput. and Inf. Sci., Finland.
- Lagerloef, G. S. E., and R. L. Bernstein (1988), Empirical orthogonal function analysis of Advanced Very High Resolution Radiometer surface temperature patterns in Santa Barbara Channel, *J. Geophys. Res.*, **93**, 6863–6873.
- Li, Z., and R. H. Weisberg (1999), West Florida continental shelf response to upwelling favourable wind forcing: 2. Dynamics, *J. Geophys. Res.*, **104**, 23,427–23,442.
- Liu, Y., and R. H. Weisberg (2005), Momentum balance diagnoses for the West Florida Shelf, *Cont. Shelf Res.*, in press.
- Liu, Y., R. H. Weisberg, and R. He (2005), Sea surface temperature patterns on the West Florida Shelf using the growing hierarchical self-organizing maps, *J. Atmos. Oceanic Technol.*, in press.
- Malmgren, B. A., and A. Winter (1999), Climate zonation in Puerto Rico based on principal components analysis and an artificial neural network, *J. Clim.*, **12**, 977–985.
- Marmorino, G. O. (1982), Wind-forced sea level variability along the West Florida shelf (winter, 1978), *J. Phys. Oceanogr.*, **12**, 389–405.
- Marmorino, G. O. (1983a), Small-scale variations of the wind-driven coastal sea level response in the West Florida Bight, *J. Phys. Oceanogr.*, **13**, 93–102.
- Marmorino, G. O. (1983b), Variability of current, temperature, and bottom pressure across the West Florida continental shelf, winter, 1981–1982, *J. Geophys. Res.*, **88**, 4439–4457.
- Mitchum, G. T., and A. J. Clarke (1986), The frictional nearshore response to forcing by synoptic scale winds, *J. Phys. Oceanogr.*, **16**, 934–946.
- Mitchum, G. T., and W. Sturges (1982), Wind-driven currents on the West Florida Shelf, *J. Phys. Oceanogr.*, **12**, 1310–1317.
- Niiler, P. P. (1976), Observations of low-frequency currents on the West Florida continental shelf, *Mem. Soc. R. Sci. Liege*, **6**, 331–358.
- Oja, M., S. Kaski, and T. Kohonen (2002), Bibliography of self-organizing map (SOM) papers: 1998–2001 addendum, *Neural Comput. Surv.*, **3**, 1–156.
- Richardson, A. J., M. C. Pfaff, J. G. Field, N. F. Silulwane, and F. A. Shillington (2002), Identifying characteristic chlorophyll a profiles in the coastal domain using an artificial neural network, *J. Plankton Res.*, **24**, 1289–1303.
- Richardson, A. J., C. Risien, and F. A. Shillington (2003), Using self-organizing maps to identify patterns in satellite imagery, *Prog. Oceanogr.*, **59**, 223–239.
- Richman, M. B. (1986), Rotation of principal components, *J. Climatol.*, **6**, 293–335.
- Risien, C. M., C. J. C. Reason, F. A. Shillington, and D. B. Chelton (2004), Variability in satellite winds over the Benguela upwelling system during 1999–2000, *J. Geophys. Res.*, **109**, C03010, doi:10.1029/2003JC001880.
- Silulwane, N. F., A. J. Richardson, F. A. Shillington, and B. A. Mitchell-Innes (2001), Identification and classification of vertical chlorophyll patterns in the Benguela upwelling system and Angola-Benguela Front using an artificial neural network, *South Afr. J. Mar. Sci.*, **23**, 37–51.
- Ultsch, A., and F. Röske (2002), Self-organizing feature maps predicting sea levels, *Inf. Sci.*, **144**, 91–125.
- Vesanto, J., J. Himberg, E. Alhoniemi, and J. Parhankangas (2000), SOM toolbox for Matlab 5, report, Helsinki Univ. of Technol., Finland.
- Weatherly, G. L., and P. J. Martin (1978), On the structure and dynamics of the oceanic bottom boundary layer, *J. Phys. Oceanogr.*, **8**, 557–570.
- Weatherly, G. L., and D. Thistle (1997), On the wintertime currents in the Florida Big Bend region, *Cont. Shelf Res.*, **17**, 1297–1319.
- Weisberg, R. H., B. D. Black, and H. Yang (1996), Seasonal modulation of the West Florida continental shelf circulation, *Geophys. Res. Lett.*, **23**, 2247–2250.
- Weisberg, R. H., Z. Li, and F. E. Muller-Karger (2001), West Florida shelf response to local wind forcing: April 1998, *J. Geophys. Res.*, **106**, 31,239–31,262.
- Weisberg, R. H., R. He, Y. Liu, and J. I. Virmani (2005), West Florida Shelf circulation on synoptic, seasonal, and inter-annual time scales, *Geophys. Monogr. Ser.*, in press.

Y. Liu and R. H. Weisberg, College of Marine Science, University of South Florida, 830 First Street South, St. Petersburg, FL 33701, USA. (yliu18@gmail.com; weisberg@marine.usf.edu)